Then, the condition

$$\left(\frac{\sqrt{\frac{ad}{bc}}-1}{\sqrt{\frac{ad}{bc}}+1}\right)^{k/2} \leq \epsilon$$

implies

$$k \geq |\log \epsilon| O\left((\underline{m}\,\underline{n})^{-1/2}\right).$$

If both $\underline{m}$ and $\underline{n}$ are $O(h^2)$, the above inequality implies

$$k \geq |\log \epsilon| O\left(\frac{1}{h^2}\right).$$

However, if one of them is $O(1)$, then

$$k \geq |\log \epsilon| O\left(\frac{1}{h}\right).$$

In the numerical experiments, we see how the bounds $\underline{m}$ and $\underline{n}$ behave with respect to changes in h and how accurate the above estimates are. We also compare the convergence of the above approach with the preconditioned GMRES by $\mathcal{P}_{\mathrm{S}}$.

4 Fill-controlled ILU matrix as a preconditioner

The iterative methods analyzed in Sects. 2 and 3 require construction of $\mathbf{Q}_B$ which should be an approximation of the Schur complement $\mathbf{S} = \mathbf{B}\mathbf{A}^{-1}\mathbf{B}^T$ or its approximation $\mathbf{B}\mathbf{Q}_A^{-1}\mathbf{B}^T$. However, as these matrices are generally dense, the computation thereof should be avoided in practice. In this section, we analyze the property of the ILU preconditioners, proposed in [14], that are not affected by this difficulty. The ILU preconditioner is represented as

$$\mathcal{P}_{\mathrm{I}} = \begin{bmatrix} \mathbf{L}_A + \mathbf{D}_A & \mathbf{0} \\ \widehat{\mathbf{B}} & \mathbf{L}_B + \mathbf{D}_B \end{bmatrix} \begin{bmatrix} \mathbf{D}_A^{-1} & \mathbf{0} \\ \mathbf{0} & -\mathbf{D}_B^{-1} \end{bmatrix} \begin{bmatrix} \mathbf{D}_A + \mathbf{L}_A^T & \widehat{\mathbf{B}}^T \\ \mathbf{0} & \mathbf{D}_B + \mathbf{L}_B^T \end{bmatrix}, \quad (55)$$

where $\mathbf{L}_A$ and $\mathbf{L}_B$ are strictly lower triangular matrices, and $\mathbf{D}_A$ and $\mathbf{D}_B$ are diagonal matrices. The nonzero pattern of $\mathbf{L}_A$ is the same as that in the lower triangular part of $\mathbf{A}$, and the nonzero pattern of $\mathbf{L}_B$ is the same as that of the lower triangular part of $\widehat{\mathbf{B}}\mathbf{D}_A^{-1}\widehat{\mathbf{B}}^T$, where the nonzero pattern of $\widehat{\mathbf{B}}$ is determined from any fill control strategy. Thus, the factorization in the second diagonal block is none other than the ILU factorization of $\widehat{\mathbf{B}}\mathbf{D}_A^{-1}\widehat{\mathbf{B}}^T$ without fill-ins, since the right hand side of Eq. (55) expands

to

$$\mathcal{P}_{\mathrm{I}} = \begin{bmatrix} (\mathbf{L}_A + \mathbf{D}_A)\mathbf{D}_A^{-1}(\mathbf{D}_A + \mathbf{L}_A^T) & (\mathbf{L}_A + \mathbf{D}_A)\mathbf{D}_A^{-1}\widehat{\mathbf{B}}^T \\ \widehat{\mathbf{B}}\mathbf{D}_A^{-1}(\mathbf{D}_A + \mathbf{L}_A^T) & \widehat{\mathbf{B}}\mathbf{D}_A^{-1}\widehat{\mathbf{B}}^T - (\mathbf{L}_B + \mathbf{D}_B)\mathbf{D}_B^{-1}(\mathbf{D}_B + \mathbf{L}_B^T) \end{bmatrix}. \tag{56}$$

We assume that all the diagonal components of $\mathbf{D}_A$ and $\mathbf{D}_B$ are positive. Then, the preconditioner can be rewritten as

$$\mathcal{P}_{\mathrm{I}} = \mathcal{T}_{\mathrm{I}}^T \begin{bmatrix} \mathbf{I} & \mathbf{0} \\ \mathbf{0} & -\mathbf{I} \end{bmatrix} \mathcal{T}_{\mathrm{I}}, \text{ with } \mathcal{T}_{\mathrm{I}} = \begin{bmatrix} \mathbf{D}_A^{-1/2}(\mathbf{D}_A + \mathbf{L}_A^T) & \mathbf{D}_A^{-1/2}\widehat{\mathbf{B}}^T \\ \mathbf{0} & \mathbf{D}_B^{-1/2}(\mathbf{D}_B + \mathbf{L}_B^T) \end{bmatrix}.$$

Hence, through the similarity transformation of the preconditioned matrix with $\mathcal{T}_{\mathrm{I}}$, we obtain

$$\begin{aligned} \mathcal{T}_{\mathrm{I}}\mathcal{P}_{\mathrm{I}}^{-1}\mathcal{A}\mathcal{T}_{\mathrm{I}}^{-1} &= \begin{bmatrix} \mathbf{I} & \mathbf{0} \\ \mathbf{0} & -\mathbf{I} \end{bmatrix} \mathcal{T}_{\mathrm{I}}^{-T}\mathcal{A}\mathcal{T}_{\mathrm{I}}^{-1} \\ &= \begin{bmatrix} \mathbf{M}_{\mathrm{I}} & \mathbf{N}_{\mathrm{I}}^T - \mathbf{M}_{\mathrm{I}}\widehat{\mathbf{N}}_{\mathrm{I}}^T \\ -(\mathbf{N}_{\mathrm{I}} - \widehat{\mathbf{N}}_{\mathrm{I}}^T\mathbf{M}_{\mathrm{I}}) & \mathbf{N}_{\mathrm{I}}\widehat{\mathbf{N}}_{\mathrm{I}}^T + \widehat{\mathbf{N}}_{\mathrm{I}}\mathbf{N}_{\mathrm{I}}^T - \widehat{\mathbf{N}}_{\mathrm{I}}\mathbf{M}_{\mathrm{I}}\widehat{\mathbf{N}}_{\mathrm{I}}^T \end{bmatrix}. \end{aligned} \tag{57}$$

Here, the following notations are used.

$$\begin{aligned} \mathbf{M}_{\mathrm{I}} &= \left((\mathbf{L}_A + \mathbf{D}_A)\mathbf{D}_A^{-1/2}\right)^{-1} \mathbf{A} \left(\mathbf{D}_A^{-1/2}(\mathbf{D}_A + \mathbf{L}_A^T)\right)^{-1}, \\ \mathbf{N}_{\mathrm{I}} &= \left((\mathbf{L}_B + \mathbf{D}_B)\mathbf{D}_B^{-1/2}\right)^{-1} \mathbf{B} \left(\mathbf{D}_A^{-1/2}(\mathbf{D}_A + \mathbf{L}_A^T)\right)^{-1}, \\ \widehat{\mathbf{N}}_{\mathrm{I}} &= \left((\mathbf{L}_B + \mathbf{D}_B)\mathbf{D}_B^{-1/2}\right)^{-1} \widehat{\mathbf{B}}\mathbf{D}_A^{-1/2}. \end{aligned}$$

From Eq. (56), we see that $\widehat{\mathbf{N}}_{\mathrm{I}} = \mathbf{N}_{\mathrm{I}}$ holds if all the fill-ins in the off-diagonal blocks are taken into account in the construction of $\widehat{\mathbf{B}}$. In this case, Eq. (57) has the same form as Eq. (43). Thus, we obtain similar eigenvalue estimations. However, considering all the fill-ins in the off-diagonal blocks is impractical. Thus, in general, we cannot ensure the positiveness of the second diagonal block in Eq. (57). Hence, we cannot guarantee that all the eigenvalues of the preconditioned matrix are contained in the right-half plane.

As in Sect. 3, we can also construct a positive version of Eq. (55) as

$$\mathcal{P}_{+\mathrm{I}} = \begin{bmatrix} \mathbf{L}_A + \mathbf{D}_A & \mathbf{0} \\ \widehat{\mathbf{B}} & \mathbf{L}_B + \mathbf{D}_B \end{bmatrix} \begin{bmatrix} \mathbf{D}_A^{-1} & \mathbf{0} \\ \mathbf{0} & \mathbf{D}_B^{-1} \end{bmatrix} \begin{bmatrix} \mathbf{D}_A + \mathbf{L}_A^T & \widehat{\mathbf{B}}^T \\ \mathbf{0} & \mathbf{D}_B + \mathbf{L}_B^T \end{bmatrix} = \mathcal{T}_{\mathrm{I}}^T\mathcal{T}_{\mathrm{I}}.$$

In this case, the similarity transformation gives

$$\mathcal{P}_{+\mathrm{I}}^{-1}\mathcal{A} \sim \mathcal{T}_{\mathrm{I}}^{-T}\mathcal{A}\mathcal{T}_{\mathrm{I}}^{-1} = \begin{bmatrix} \mathbf{M}_{\mathrm{I}} & \mathbf{N}_{\mathrm{I}}^T - \mathbf{M}_{\mathrm{I}}\widehat{\mathbf{N}}_{\mathrm{I}}^T \\ \mathbf{N}_{\mathrm{I}} - \widehat{\mathbf{N}}_{\mathrm{I}}^T\mathbf{M}_{\mathrm{I}} & -(\mathbf{N}_{\mathrm{I}}\widehat{\mathbf{N}}_{\mathrm{I}}^T + \widehat{\mathbf{N}}_{\mathrm{I}}\mathbf{N}_{\mathrm{I}}^T - \widehat{\mathbf{N}}_{\mathrm{I}}\mathbf{M}_{\mathrm{I}}\widehat{\mathbf{N}}_{\mathrm{I}}^T) \end{bmatrix}.$$

Once again, we cannot theoretically bound the eigenvalue distribution of the second diagonal block in the negative region.

5 Numerical experiments

We now examine the performance of the preconditioners introduced in Sects. 3 and 4. The problem tested is a deformation problem of the so-called Mooney–Rivlin body, for which the deformation potential per unit volume is given by

$$W(\mathbf{C}) = c_1\widehat{\mathrm{I}}_C + c_2\widehat{\mathrm{II}}_C. \tag{58}$$

Here, $\mathbf{C}$ is the right Cauchy Green deformation tensor defined as

$$\mathbf{C} = \left(\mathbf{I} + \frac{\partial \mathbf{u}}{\partial \mathbf{X}}\right)^T \left(\mathbf{I} + \frac{\partial \mathbf{u}}{\partial \mathbf{X}}\right),$$

where $\mathbf{X}$ is the position vector in the undeformed configuration, and $\mathbf{u} = \mathbf{u}(\mathbf{X})$ is the displacement vector of the material point $\mathbf{X}$ after the deformation. The invariants are defined as

$$\begin{aligned}\widehat{\mathrm{I}}_C &= \det(\mathbf{C})^{-1/3}\mathrm{tr}(\mathbf{C}),\\ \widehat{\mathrm{II}}_C &= \det(\mathbf{C})^{-2/3}\left(\mathrm{tr}(\mathbf{C})^2 - \mathrm{tr}(\mathbf{C}^2)\right).\end{aligned}$$

In the above case, we solve the variational problem for the energy functional:

$$E = \int_\Omega W(\mathbf{C})d\Omega$$

with the incompressibility constraint, $\det(\mathbf{C}) - 1 = 0$. Here, Ω is the domain of material in the undeformed configuration. The constraint variational problem described in Eqs. (5) and (6) is represented by the following weak formulation:

$$\int_\Omega \left(\frac{\partial W}{\partial \mathbf{C}} + \lambda \det(\mathbf{C})\mathbf{C}^{-1}\right) : \frac{\partial \mathbf{C}}{\partial \mathbf{u}}\delta\mathbf{u}d\Omega = 0, \quad \forall\delta\mathbf{u} \tag{59}$$

$$\int_\Omega \delta\lambda(\det(\mathbf{C}) - 1)d\Omega = 0, \ \forall\delta\lambda. \tag{60}$$

The notation ':' denotes the standard dot product of the tensors, and we apply the formula:

$$\frac{\partial \det(\mathbf{C})}{\partial \mathbf{C}} = \det(\mathbf{C})\mathbf{C}^{-1}.$$

As described in Sect. 1, Eqs. (59) and (60) are further linearized to perform the Newton–Raphson iterations, and we have to solve the system of linear equations given in Eqs. (8) and (9).

When applying a finite element discretization to constraint problems, we have to be mindful of the stability of the discretized linear system with respect to the applied finite element interpolations to the displacement $\mathbf{u}$ and the Lagrange multiplier λ [4]. To ensure stability, we adopt the so-called mini element [1], in which a central displacement node is added to each triangular or tetrahedral element and the Lagrange multiplier nodes are placed on the vertices.

In the inexact block LU preconditioner defined in Eq. (11), we need to determine the matrices $\mathbf{Q}_A$ and $\mathbf{Q}_B$, where $\mathbf{Q}_A$ should be an approximation of $\mathbf{A}$. Thus, we adopt the ILU factorization without fill-in:

$$\mathbf{Q}_A = (\mathbf{L}_A + \mathbf{D}_A)\mathbf{D}_A^{-1}(\mathbf{D}_A + \mathbf{L}_A^T). \tag{61}$$

Note that $\mathbf{L}_A$ and $\mathbf{D}_A$ are the same matrices that appeared in the first block of the ILU factorization in Eq. (55) of the whole matrix $\mathcal{A}$. According to Lemma 5, $\mathbf{Q}_B$ is preferably a good approximation of $\mathbf{B}\mathbf{Q}_A^{-1}\mathbf{B}^T$. Though it is easy to perform the matrix multiplication by $\mathbf{B}\mathbf{Q}_A^{-1}\mathbf{B}^T$ of any given vector, the direct computation of the components of $\mathbf{B}\mathbf{Q}_A^{-1}\mathbf{B}^T$ leads to a dense matrix. Hence, to work with only sparse matrices, we again adopt the factorization in Eq. (55) as

$$\mathbf{Q}_B = (\mathbf{L}_B + \mathbf{D}_B)\mathbf{D}_B^{-1}(\mathbf{D}_B + \mathbf{L}_B^T), \tag{62}$$

based on the following consideration. From Eq. (56), $\mathbf{Q}_B$ in Eq. (62) is expected to be an approximation of $\widehat{\mathbf{B}}\mathbf{D}_A^{-1}\widehat{\mathbf{B}}^T$. And again from the off-diagonal part in the same equation, $(\mathbf{L}_A + \mathbf{D}_A)\mathbf{D}_A^{-1}\widehat{\mathbf{B}}^T$ is expected to be an approximation of $\mathbf{B}^T$. Thus, the following chain of approximative relations holds.

$$\mathbf{B}\left\{(\mathbf{L}_A + \mathbf{D}_A)\mathbf{D}_A^{-1}(\mathbf{D}_A + \mathbf{L}_A^T)\right\}^{-1}\mathbf{B}^T \approx \widehat{\mathbf{B}}\mathbf{D}_A^{-1}\widehat{\mathbf{B}}^T \approx (\mathbf{L}_B + \mathbf{D}_B)\mathbf{D}_B^{-1}(\mathbf{D}_B + \mathbf{L}_B^T)$$

As for the fill control to construct $\mathbf{Q}_A$ by factorizing $\mathbf{A}$, all fill-ins are ignored. Also, in the factorization of $\widehat{\mathbf{B}}\mathbf{D}_A^{-1}\widehat{\mathbf{B}}^T$ to construct $\mathbf{Q}_B$, we do not allow any fill-ins. However, in the factorization at the off-diagonal block to compute $\widehat{\mathbf{B}}$, we test both level 1 fill-ins and the no fill-in case. We denote these preconditioners by $\mathcal{P}_S(L)$ and $\mathcal{P}_I(L)$, where L is the fill-in level allowed for $\widehat{\mathbf{B}}$.

We now examine the performance of the preconditioners $\mathcal{P}_S(L)$ and $\mathcal{P}_I(L)$ with linear systems arising from a deformation analysis by a simple stretch, in which the undeformed configuration is either a unit square or a unit cube as depicted in Fig. 2. Due to the symmetry of geometry, we compute only one half of the actual material in each direction. For example, the following boundary conditions are imposed on the displacement vector function $\mathbf{u} = (u_1, u_2, u_3)^T$ in the case of the cube.

$u_1 = u_2 = 0$, $u_3 = D_3$ on $\{X_3 = 1\}$: (the top), $u_3 = 0$ on $\{X_3 = 0\}$: (the bottom),
$u_1 = 0$ on $\{X_2 = 0\}$, $u_2 = 0$ on $\{X_1 = 0\}$: (the side walls).

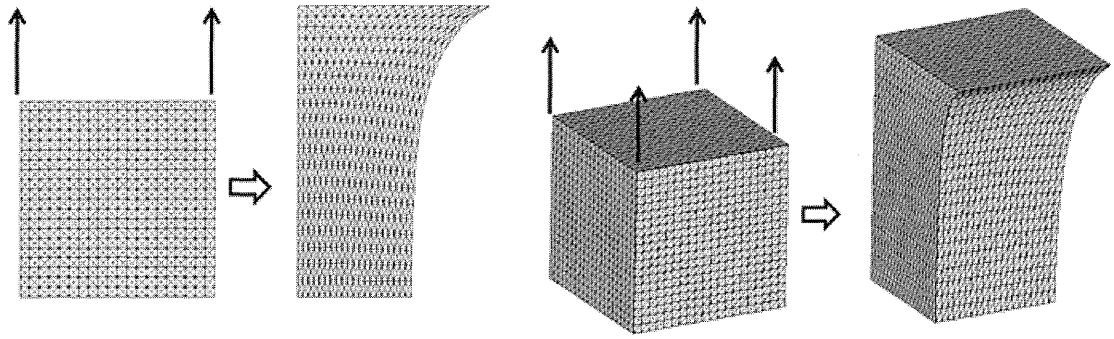

Fig. 2 The initial and final configurations of the two-dimensional 20^2 mesh (*left*) and three-dimensional 20^3 mesh (*right*)

Table 1 The degrees of freedom (D.O.F.) and the number of nonzero components in the matrix (nz($\mathcal{A}$))

Mesh size	D.O.F.	nz($\mathcal{A}$)
Two-dimensional problem		
20^2	5,640	111,686
40^2	22,480	452,166
80^2	89,760	1,819,526
Three-dimensional problem		
10^3	26,510	2,324,764
20^3	206,020	19,201,294

Fig. 3 Arnoldi procedure for $\mathcal{A}\mathcal{P}^{-1}$

$v_1 = r_0 (= b - \mathcal{A}u_0)$; $v_1 = v_1 / \|v_1\|$
for $i = 1, \ldots, m$;
  $w_i = \mathcal{A}\mathcal{P}^{-1} v_i$;
  for $j = 1, \ldots, i$;
    $h_{j,i} = (w_i, v_j)$; $w_i = w_i - h_{j,i} v_j$;
  next j;
  $h_{i+1,i} = \|w_i\|$; $v_{i+1} = w_i / h_{i+1,i}$;
next i;

The magnitude of stretch D_3 is increased by 0.1 in each step up to $D_3 = 0.5$. Thus, five incremental steps are required to reach the final configuration. As for the material parameters in Eq. (58), $c_1 = 0.3, c_2 = 0.15$ are adopted. The number of elements adopted in each direction is either 20, 40 or 80 in the two-dimensional case, and 10 or 20 in the three-dimensional case. The total degrees of freedom, except for the imposed boundary condition and the number of nonzero components in the coefficient matrix, are given in Table 1. Note that even though the matrices are sparse, there are nearly twenty and a hundred nonzeros in each row in the two- and three-dimensional cases, respectively.

In the linear solutions, we adopted the right-preconditioned full GMRES. The preconditioned GMRES algorithm is based on the Arnoldi procedure [12], in which the orthonormal basis $\{v_i\}_{i=1,\ldots,m}$ is constructed for the preconditioned matrix $\mathcal{A}\mathcal{P}^{-1}$ as described in Fig. 3.

By inspecting the Hessenberg matrix defined by

$$H(m) = (h_{j,i})_{i,j=1,m} = ((\mathcal{A}\mathcal{P}^{-1}v_j, v_i))_{i,j=1,m}, \quad (h_{j,i} = 0 \quad \text{for } i+1 < j),$$

we can see how the matrix $\mathcal{A}\mathcal{P}^{-1}$ acts on the Krylov subspace spanned by the basis vectors $v_1, \ldots, v_m$. Thus, at the final solution stage, we extracted the Hessenberg matrix $H(m)$ (where m is the number of iterations) and examined its eigenvalue distribution. Table 2 gives the bounds of the eigenvalue distribution, the average number of GMRES iterations in one solution process, and the average CPU time in one solution process. In the experiment, each GMRES iteration was stopped when the relative L2-norm of the residual was smaller than 10^{-8}. For each increment of the displacement, on average four Newton–Raphson iterations were required before the nonlinear equation converged. The computation was performed with a single CPU (Intel(R) Pentium(R) model 4, Clock 3.4 GHz, Cache size 16 kB, Main memory 2 GB). To validate the estimates in Eq. (48) of the eigenvalues with nonzero imaginary parts for $\mathcal{P}_S$, we picked an eigenvalue $\widehat{\lambda}$ that satisfies

$$\mathrm{Re}(\widehat{\lambda}) = \min\{\mathrm{Re}(\lambda) \mid \mathrm{Im}(\lambda) \neq 0\}.$$

The following observations together with their interpretations associated with the theory in Sects. 3 and 4 were made.

1. Minimal real part of the eigenvalues
   In all cases, these minimums are given on the real axis. The values are the same for all preconditioners for a common mesh size. The order of these is obviously h^2, where h indicates the element size. For $\mathcal{P}_S$, these minimums can possibly be determined only from $\underline{m}$ in Eq. (47), since the minimums are the same for the different fill levels of $\widehat{\mathbf{B}}$ which causes the change in $\mathbf{N}$, and thus also the change in $\underline{n}$.
2. Maximal real parts of the eigenvalues
   These are almost independent of the element size. In the case of $\mathcal{P}_S$, they are larger than 2, but decrease with an increase in the fill-in level. This indicates that they are determined from $\overline{n}$ in Eq. (47). It also means that using $\mathcal{P}_S$ in the matrix splitting iterations in Sect. 2 leads to the divergence. We can apply an appropriate scaling factor to $\mathbf{Q}_B$ so that the condition in Eq. (42) in Theorem 4 is satisfied. However, this does not bring about any meaningful convergence improvement in the use as a preconditioner in these examples. The decrease in the maximums with the associated increase in the fill-in level in $\widehat{\mathbf{B}}$ is brought about by the improvement in the approximation of $\widehat{\mathbf{B}}\mathbf{Q}_A\mathbf{B}^T$ by $\mathbf{Q}_B$ that leads to the decrease in $\overline{n}$. For $\mathcal{P}_I$, the maximums are well bounded, although they increased slightly when the fill-ins were applied.
3. Bounds for the imaginary parts of the eigenvalues
   For $\mathcal{P}_S$, the bounds are much smaller than one and almost independent of the element size and the fill-in level in $\widehat{\mathbf{B}}$. We cannot give a good explanation for this insensitivity to the fill-in level based on the current theory. On the other hand, the bounds are greater than one for $\mathcal{P}_I(0)$. But, the bounds are improved in $\mathcal{P}_I(1)$.

4. Eigenvalues with negative real parts
   As predicted in Theorem 4, all the eigenvalues are included in the right half plane for $\mathcal{P}_S$. However, for $\mathcal{P}_I$ there are a few eigenvalues outside this plane, and these disappear if the fill-ins in $\widehat{\mathbf{B}}$ are applied in some cases. This reflects the inherent difficulty in judging the positiveness of the matrix $\mathbf{N}_I\widehat{\mathbf{N}}_I^T + \widehat{\mathbf{N}}_I\mathbf{N}_I^T - \widehat{\mathbf{N}}_I\mathbf{M}_I\widehat{\mathbf{N}}_I^T$ in Eq. (57). Note that the imaginary parts of these eigenvalues are not that small and as such, they may not affect the convergence rate too severely.
5. Convergence and execution time
   The dependence of the number of iterations on element size h is slightly larger than $O(1/h)$ for both preconditioners. However, it is much smaller than $O(1/h^2)$. There is no complete theory to explain this convergence behavior. However, this tendency of $\mathcal{P}_S$ seems to be closely related to the distribution of eigenvalues with

Table 2 The eigenvalue distribution bounds in the right-half plane at the final equilibrium, eigenvalues in the left-half plane if they exist in column 'negative Re', and the average number of GMRES iterations and solution times

Prec.	Mesh	min Re(λ)	max Re(λ)	max Im(λ)	$\widehat{\lambda}$	Negative Re
Two-dimensional triangular mesh (eigenvalue distribution)						
$\mathcal{P}_S(0)$	20	0.016	10.6	0.44	(0.069, ±0.22)	None
	40	0.0041	10.6	0.45	(0.018, ±0.11)	None
	80	0.0010	10.6	0.47	(0.0047, ±0.057)	None
$\mathcal{P}_I(0)$	20	0.016	1.68	1.26	–	(−0.011, ±0.51)
	40	0.0041	1.70	1.24	–	(−0.083, ±0.26)
	80	0.0010	1.71	1.24	–	(−0.044, ±0.13) (−0.046, ±0.13) (−0.0099, ±0.56)
$\mathcal{P}_S(1)$	20	0.016	4.7	0.45	(0.10, ±0.27)	None
	40	0.0041	4.6	0.47	(0.026, ±0.14)	None
	80	0.0010	4.6	0.47	(0.0066, ±0.071)	None
$\mathcal{P}_I(1)$	20	0.016	1.82	0.77	–	None
	40	0.0041	1.84	0.74	–	(−0.0096, ±0.24)
	80	0.0010	1.84	0.74	–	(−0.014, ±0.12)
Three-dimensional tetrahedral mesh (eigenvalue distribution)						
$\mathcal{P}_S(0)$	10	0.010	5.52	0.44	(0.11, ±0.0017)	None
	20	0.0025	5.53	0.46	(0.082, ±0.25)	None
$\mathcal{P}_I(0)$	10	0.010	1.51	1.06	–	(−0.076, ±0.73) (−0.099, ±0.33)
	20	0.0025	1.53	0.97	–	(−0.0052, ±0.49)
$\mathcal{P}_S(1)$	10	0.010	3.09	0.35	(0.74, ±0.36)	None
	20	0.0025	3.17	0.46	(0.21, ±0.37)	None
$\mathcal{P}_I(1)$	10	0.010	1.60	0.76	–	None
	20	0.0025	1.64	0.65	–	None

Table 2 Continued

Iterations and solution times			
Prec.	Mesh	♯IT	Time (s)
Two-dimensional triangular mesh			
$\mathcal{P}_{\mathrm{S}}(0)$	20	78	0.31
	40	165	3.39
	80	374	48.5
$\mathcal{P}_{\mathrm{I}}(0)$	20	84	0.26
	40	192	3.37
	80	459	58.2
$\mathcal{P}_{\mathrm{S}}(1)$	20	62	0.27
	40	129	2.52
	80	287	33.0
$\mathcal{P}_{\mathrm{I}}(1)$	20	59	0.23
	40	134	2.45
	80	315	34.7
Three-dimensional tetrahedral mesh			
$\mathcal{P}_{\mathrm{S}}(0)$	10	100	4.55
	20	227	120
$\mathcal{P}_{\mathrm{I}}(0)$	10	113	3.79
	20	275	130
$\mathcal{P}_{\mathrm{S}}(1)$	10	78	4.30
	20	169	90.0
$\mathcal{P}_{\mathrm{I}}(1)$	10	76	5.29
	20	170	105

The fill level for $\widehat{B}$ is indicated in parentheses in column 'Prec'

nonzero imaginary parts. This is discussed further when we compare the convergence with the positive preconditioner $\mathcal{P}_{+\mathrm{S}}$. In general, the convergence with $\mathcal{P}_{\mathrm{S}}$ is substantially better than with $\mathcal{P}_{\mathrm{I}}$, and the difference becomes larger with an increase in mesh size $O(1/h)$. The convergence deterioration with $\mathcal{P}_{\mathrm{I}}$ may be as a result of the presence of those eigenvalues not included in the right-half plane, since a fairly similar convergence is observed when they disappear with the fill-ins.

Next, in addition to observing the simple bounds of the eigenvalues in the table, we examine the distribution in greater detail, in particular, focusing the eigenvalues around the origin. The eigenvalue distributions for $\mathcal{P}_{\mathrm{S}}(0)$, $\mathcal{P}_{\mathrm{S}}(1)$ and $\mathcal{P}_{\mathrm{I}}(0)$, $\mathcal{P}_{\mathrm{I}}(1)$ in the 80^2 square problem are depicted in Fig. 4. The plots on the left show the global distributions, while those on the right show the local distributions around the origin in the right-half plane. For comparison with the estimation of the imaginary part in Eq. (49), the curve defined by $x = y^2$ is also depicted. The results for $\mathcal{P}_{\mathrm{S}}$ show that

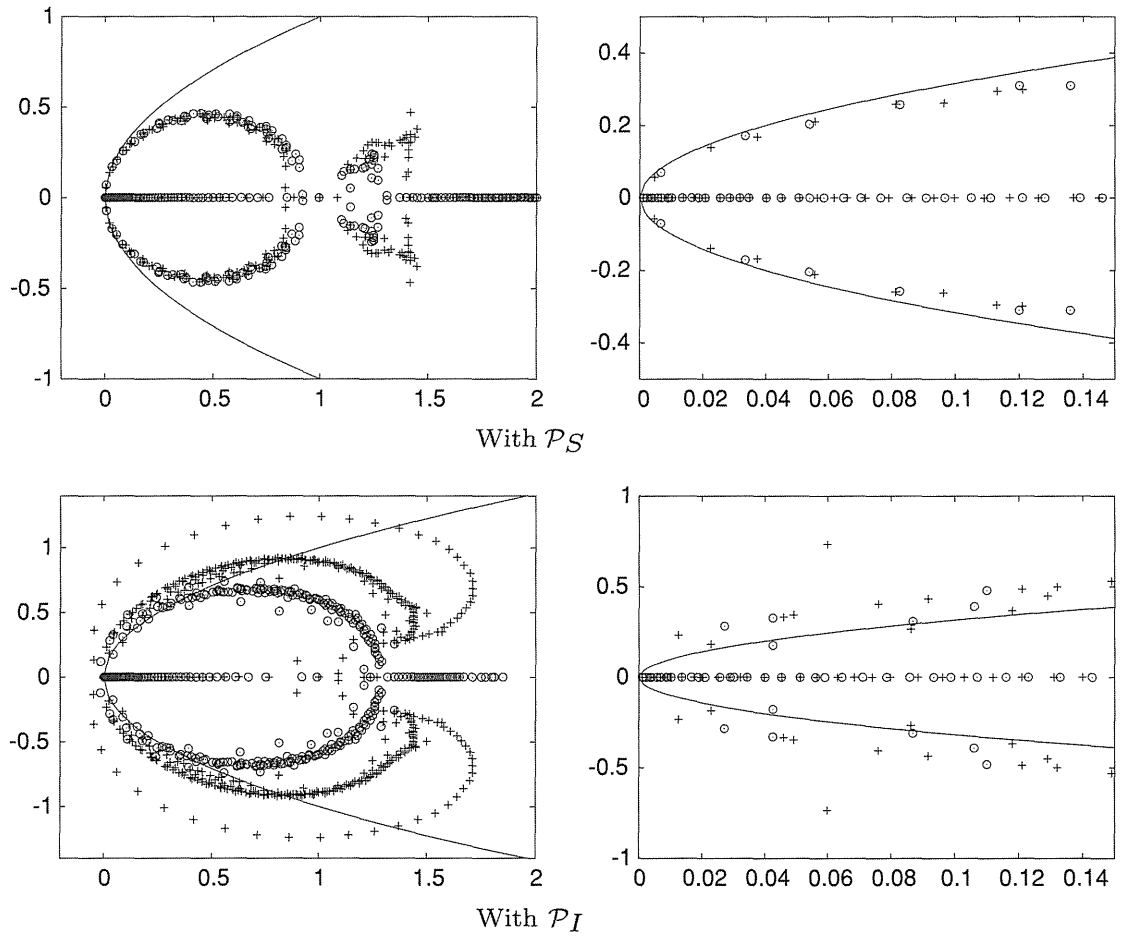

Fig. 4 Eigenvalue distributions for the two-dimensional problem (80^2). *Plus symbol* and *open circle* indicate fill levels of 0 and 1, respectively. The *solid line* shows the curve $y^2 = x$

Eq. (49) provides an exact estimate of the magnitude of the imaginary part around the origin. On the other hand, most of the eigenvalues are out of the bounds around the origin for $\mathcal{P}_{\mathrm{I}}$. This indicates difficulties of theoretical prediction for the convergence performance of $\mathcal{P}_{\mathrm{I}}$. However, $\mathcal{P}_{\mathrm{I}}$ realizes comparable convergence speed to $\mathcal{P}_{\mathrm{S}}$ as we will see later in this section.

Since there does not appear to be any theory that can explain the almost $\mathrm{O}(1/h)$ convergence rate for $\mathcal{P}_{\mathrm{S}}$ from the eigenvalue distribution, we validate the applicability of Eq. (54) for the positive symmetric preconditioner $\mathcal{P}_{+\mathrm{S}}$. Table 3 gives the eigenvalue bounds $[-a, -b] \cup [c, d]$ for the Hessenberg matrix for $\mathcal{A}\mathcal{P}_{+\mathrm{S}}(1)^{-1}$ and the average number of GMRES iterations for the two-dimensional case. Note that here we can basically apply MINRES instead of GMRES to reduce the computational cost of the dot products. However, as we are interested in the comparison of the convergence rate with the GMRES iteration preconditioned by $\mathcal{P}_{\mathrm{S}}(1)$, GMRES is applied to $\mathcal{A}\mathcal{P}_{+\mathrm{S}}(1)^{-1}$. The upper bound $-b$ in the negative region seems to decrease with order h, while the lower bound c in the positive region decreases with order h^2. According to Eq. (54), this results in an order for the number of iterations of $(1/h)^{3/2}$. A similar estimate was obtained by Wathen for a block diagonal preconditioner for the Stokes equation [16]. However, a simple calculation from the number of iterations in the table,

Table 3 Comparison of the eigenvalue bounds and the convergence for $P_{+S}(1)$ and $P_S(1)$ in the two-dimensional case

Mesh size	$-a$	$-b$	c	d	♯IT
$\mathcal{P}_{+S}$					
20	−5.3	−0.37	0.016	1.7	150
40	−5.3	−0.16	0.0041	1.8	333
80	−5.3	−0.075	0.0010	1.9	691
Mesh size	min Re(λ)	max Re(λ)	$\widehat{\lambda}$	♯IT	
$\mathcal{P}_S$					
20	0.016	4.7	(0.10, ±0.27)	62	
40	0.0041	4.6	(0.026, ±0.14)	129	
80	0.0010	4.6	(0.0066, ±0.071)	287	

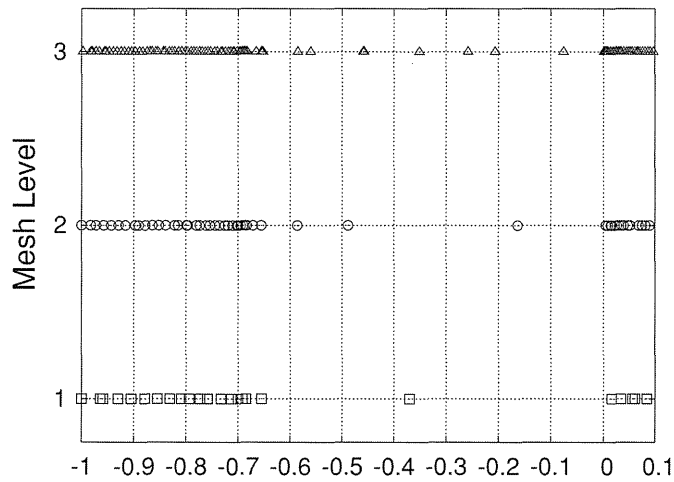

Fig. 5 Eigenvalue distributions on the real axis for the three mesh levels (1:20^2, 2:40^2, 3:80^2)

such as

$$150 \cdot 2^{3/2} \approx 424 \gg 333, \quad 333 \cdot 2^{3/2} \approx 942 \gg 691,$$

indicates faster convergence than that predicted from the theory. The reason for the discrepancy in this convergence estimate may be better understood if we look more closely at the eigenvalue distribution depicted in Fig. 5. The interesting thing here is that there is a common border over all the mesh levels where the dense and sparse distributions in the negative region are separated. Although the number of eigenvalues in the sparse part increases with an increase in the mesh level, their distribution is still much sparser compared with the dense part. This certainly brings about a faster convergence than the previous prediction. The reason of this tendency in the eigenvalue distributions is not entirely clear at the moment. According to the theory, it seems to be related to the eigenvalue distribution of $\mathbf{N}\mathbf{N}^T \sim \mathbf{Q}_B^{-1}\mathbf{B}\mathbf{Q}_A^{-1}\mathbf{B}^T$.

It is also interesting to compare the convergence rate with $\mathcal{P}_S$. The numbers of iterations with $\mathcal{P}_{+S}$ are more than double those with $\mathcal{P}_S$. In the extreme case where the

Table 4 Comparison of the convergence of the first diagonal block matrix $\mathbf{A}$ and the whole matrix $\mathcal{A}$

Mesh size	$\mathbf{Q}_A$ for $\mathbf{A}$		$\mathcal{P}_S(1)$ for $\mathcal{A}$		$\mathcal{P}_I(1)$ for $\mathcal{A}$	
	♯IT	Time (s)	♯IT	Time (s)	♯IT	Time (s)
20^2	53	0.091	62	0.27	59	0.23
40^2	104	0.82	129	2.52	134	2.45
80^2	201	9.55	287	33.0	315	34.7
10^3	84	3.96	78	5.29	76	4.30
20^3	162	49.2	169	90.0	170	105

exact block LU factorization (i.e. $\mathbf{Q}_A = \mathbf{A}$, $\mathbf{Q}_B = \mathbf{S}$) is applied, the preconditioned matrix for the former is similar to $\widetilde{\mathcal{E}}$ defined in Eq. (30), whereas for the latter it is the identity matrix. This may explain the tendency above. We cannot, however, give any reasonable explanation for this relation in the inexact block LU factorization case, because the Krylov subspace, produced by each of these, is different.

Finally, we compare the convergence of the whole matrix with that of only the first diagonal block $\mathbf{A}$. In this comparison, we extracted the first diagonal block $\mathbf{A}$ and F from the whole system in Eq. (1) and solved $\mathbf{A}X = F$ using the GMRES iteration with the preconditioner $\mathbf{Q}_A$ in each Newton–Raphson step. Note that we applied GMRES to the positive symmetric problems, since we are interested in the comparison of the GMRES iteration for the whole system. In Table 4, the average number of iterations and the CPU time are compared. These results imply reasonable performance of the proposed preconditioners for the whole system. In particular, the number of iterations is almost the same for the three-dimensional problem.

6 Conclusions

The main objective of this study was to explore the inexact LU-type preconditioners for saddle point problems arising in nonlinear continuum analysis. Many of the previous studies on saddle point problems assumed that good preconditioners, $\mathbf{Q}_A$ for $\mathbf{A}$ or $\mathbf{Q}_B$ for $\mathbf{S}$, were available. However, in real-life applications of finite element analysis for hyper-elastic materials, this requirement is too strict since we do not have a good understanding of the properties of the resultant matrices $\mathbf{A}$ and $\mathbf{B}$ and they usually do not have any hierarchical structure which makes the application of multilevel methods easier. Thus, it is important to construct the best preconditioner for the whole system with the available approximative matrices $\mathbf{Q}_A$ and $\mathbf{Q}_B$. From this point of view, we have tried to make exact estimates of the eigenvalue distribution and to understand the convergence behavior using an approximation $\mathbf{Q}_A$ which is not spectrally equivalent to $\mathbf{A}$. We have shown that we can achieve almost order $1/h$ for the number of iterations before convergence by constructing $\mathbf{Q}_A$ and $\mathbf{Q}_B$ from the simple ILU factorizations. Although our theoretical explanation for this convergence rate is still incomplete, we have provided a good starting point for further development of the theory. Furthermore, such a theoretical consideration will certainly bring about further improvements

in preconditioning techniques for use in the area of highly nonlinear incompressible continuum analysis.

References

1. Arnold, D.N., Brezzi, F., Fortin, M.: A stable finite element for stokes equations. Calcolo **21**, 337–344 (1984)
2. Benzi, M., Golub, G.H., Liesen, J.: Numerical solution of saddle point problems. Acta Numerica **14**, 1–137 (2005)
3. Bramble, J.H., Pasciak, J.E., Vassilev, A.T.: Analysis of the inexact Uzawa algorithm for saddle point problems. SIAM Numer. Anal. **34**, 1072–1092 (1997)
4. Brezzi, F., Bathe, K.J.: A discourse on the stability conditions for mixed finite element formulations. Comput. Methods Appl. Mech. Eng. **82**, 27–57 (1990)
5. Elman, H.C., Silvester, D.J., Wathen, A.J.: Performance and analysis of saddle point preconditioners for the discrete steady-state Navier-Stokes equations. Numer. Math. **90**, 641–664 (2002)
6. Elman, H.C., Silvester, D.J., Wathen, A.J.: Finite Elements and Fast Iterative Solvers. Numerical Mathematics and Scientific Computation. Oxford University Press, Oxford (2005)
7. Greenbaum, A.: Iterative Methods for Solving Linear Systems. Frontiers in Applied Mathematics, vol. 17. SIAM, Philadelphia (1997)
8. Klawonn, A., Starke, G.: Block triangular preconditioners for nonsymmetric saddle point problems: field-of-values analysis. Numer. Math. **81**, 577–594 (1999)
9. Little, L., Saad, Y., Smoch, L.: Block preconditioners for symmetric and nonsymmetric saddle point problems. SIAM J. Sci. Comput. **25**, 729–748 (2003)
10. Mardal, K.A., Winther, R.: Uniform preconditioners for the time dependent Stokes problem. Numer. Math. **98**, 305–327 (2004)
11. Paige, C.C., Saunders, M.A.: Solution of sparse indefinite systems of linear equations. SIAM J. Numer. Anal. **12**, 617–629 (1975)
12. Saad, Y., Shultz, M.H.: GMRES: a generalized minimal residual algorithm for solving nonsymmetric linear systems. SIAM J. Sci. Comput. **7**, 856–869 (1986)
13. Silvester, D.J., Wathen, A.J.: Fast iterative solution of stabilised Stokes systems part II: using general block preconditioners. SIAM J. Numer. Anal. **31**, 1352–1367 (1994)
14. Washio, T., Hisada, T., Watanabe, H., Tezduyar, T.E.: A robust and efficient iterative linear solver for strongly coupled fluid-structure interaction problems. Comput. Methods Appl. Mech. Eng. **194**, 4027–4047 (2005)
15. Wathen, A.J., Silvester, D.J.: Fast iterative solution of stabilised Stokes systems part I: using simple diagonal preconditioners. SIAM J. Numer. Anal. **30**, 630–649 (1993)
16. Wathen, A.J., Fischer, B., Silvester, D.J.: The convergence rate of the minimal residual method for the Stokes problem. Numer. Math. **71**, 121–134 (1995)

33rd Annual International Conference of the IEEE EMBS
Boston, Massachusetts USA, August 30 - September 3, 2011

Reduction of Myocardial Oxygen Demand by Controlling Heart Rate and Hemodynamics Simultaneously by Novel Circulatory Model

Masaru Sugimachi, *Member*, *IEEE*, Kazunori Uemura, Toru Kawada, Toshiaki Shishido, and Kenji Sunagawa, *Member*, *IEEE*

Abstract—**We were already capable of restoring automatically blood pressure, cardiac output, and left atrial pressure by an inotropic, a vasodilator, and volume infusion/a diuretic. Countermeasures for cardioprotection, however, should be integrated to improve the long-term outcomes. We established a full control of heart rate and examined if such a control was useful for decreasing cardiac oxygen consumption. Based on a simulation result, we conducted an animal experiment. In 7 dogs with acute heart failure, we treated hemodynamics, and then lowered heart rate. Compared to the treatment for hemodynamics alone, the addition of bradycardia decreased cardiac oxygen consumption. It was possible to maintain hemodynamics without sacrificing cardiac oxygen consumption.**

I. Introduction

THE ultimate goal of the treatment of acute failure is the restoration of failing hemodynamics. Although the native regulation for the cardiovascular system plays a role to sustain normal blood pressure when the severity of heart failure is mild (called compensated heart failure), the ability of native regulation is limited. To sustain life, not only blood pressure, but also peripheral perfusion (indexed by cardiac output) and the absence of pulmonary edema (indexed by low left atrial pressure) are necessary. The native regulation fails to restore cardiac output and left atrial pressure in advanced heart failure.

We have shown that with the use of an inotropic agent, a vasodilator, and volume infusion/a diuretic, we were able to restore automatically all of blood pressure, cardiac output, left atrial pressure [1]. In this study, the peripheral demand was fulfilled. The overload on the heart was, however, not ameliorated. Countermeasures for cardioprotection should probably also be a part of the treatment and should be integrated, so as to improve the long-term outcomes of the patient recovering from acute heart failure.

Manuscript received April 13, 2011. This work was supported in part by Grant-in-Aid for Scientific Research (B 20300164) from the Ministry of Education, Culture, Sports, Science and Technology, by Health and Labour Sciences Research Grants (H20-katsudo-shitei-007) from the Ministry of Health Labour and Welfare of Japan (corresponding author Masaru Sugimachi, MD, PhD to provide phone: +81-6-6833-5012; fax: +81-6-6835-5403; e-mail: su91mach@ri.ncvc.go.jp).

M. Sugimachi, K. Uemura, T. Kawada, and T. Shishido are with the National Cerebral and Cardiovascular Center Research Institute, Suita, Osaka 5658565, Japan.

K. Sunagawa is with Kyushu University, Fukuoka 8128582 Japan.

We have already used the control of left ventricular contractility, systemic vascular resistance and blood volume to automatically restore blood pressure, cardiac output, and left atrial pressure. For the cardioprotection, we have to use the control of another cardiovascular property. We focused on the control of heart rate and examined if this was useful for the cardioprotection. We assumed here that low minute left ventricular oxygen consumption can be used as an index for cardioprotection.

II. Theoretical Analysis

A. Definition of the Problem

To supply the peripheral demand and to prevent pulmonary congestion, the cardiovascular system needs to operate with sufficiently high mean blood pressure (P_m), large cardiac output (CO), and low left atrial pressure (P_{LA}). Considering the physiologically normal values, we fixed P_m to 100 mmHg, CO to 100 $ml \cdot min^{-1} \cdot kg^{-1}$, and P_{LA} to 10 mmHg.

Even with these multiple constraints, the cardiovascular system does not operate with a unique condition. It can operate with various sets of contractility and heart rate (*see the next subsection B*). We simulated these various hemodynamics, and searched for the condition to minimize minute LV oxygen consumption [2].

B. Hemodynamics

We used left ventricular (LV) end-systolic pressure-volume relationship (ESPVR) and the framework of ventricular-arterial coupling to reproduce hemodynamics [3]. We approximated LV ESPVR by a straight line, and coupled end-systolic elastance (E_{es}) with effective arterial elastance (E_a). E_a was approximated by R/T, where R was systemic vascular resistance and T was heart period, reciprocal of heart rate (HR).

Using these approximations, for a given LV end-diastolic stressed volume (V_{eds}), stroke volume (SV) and CO can be calculated as

$$SV = V_{eds} \frac{T \cdot E_{es}}{T \cdot E_{es} + R} \quad (1)$$

$$CO = V_{eds} \frac{E_{es}}{T \cdot E_{es} + R} \quad (2).$$

LV end-systolic stressed volume (V_{ess}) and pressure (P_{es})

can be calculated as

$$V_{ess} = V_{eds} \frac{R}{T \cdot E_{es} + R} \quad (3)$$

$$P_{es} = V_{eds} \frac{E_{es} \cdot R}{T \cdot E_{es} + R} \quad (4).$$

In the framework of ventricular-arterial coupling, P_m was approximated by P_{es}. Systemic vascular resistance, R was therefore given by 1 mmHg·ml^{-1}·min·kg. Also, as P_{LA} was approximated by LV end-diastolic pressure (P_{ed}), V_{eds} would be calculated if we assume a predefined LV end-diastolic pressure-volume relationship (EDPVR). In this analysis, we used an exponential LV EDPVS as follows (V_{eds} in mL, P_{ed} in mmHg)

$$P_{ed} = \exp(0.082 \cdot V_{eds} - 0.8) + 2.03 \quad (5),$$

corresponding to the EDPVR with P_{ed} of 10 mmHg for V_{eds} of 35 ml.

Knowing R and V_{eds}, a necessary relationship between LV contractility (E_{es}) and heart period (T, an inverse of heart rate) is obtained. Even though it is necessary to follow this relationship to maintain P_m, CO, and P_{LA}, not a unique set of E_{es} and T would be obtained. Rather multiple sets of E_{es} and T would be feasible (*see the previous subsection A*).

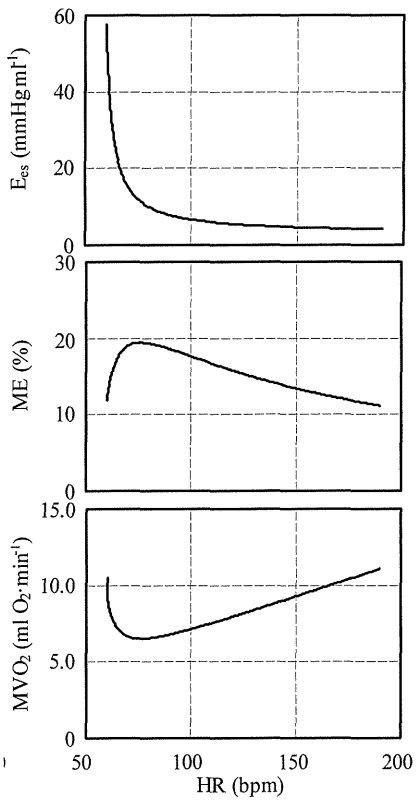

Fig. 1. Simulated relations of heart rate (HR) with left ventricular end-systolic elastance (E_{es}) (top), left ventricular mechanical efficiency (ME) (middle), and minute left ventricular oxygen consumption (MVO_2) (bottom), when mean blood pressure, cardiac output and left atrial pressure are kept at fixed values

C. Myocardial Oxygen Consumption

Beat LV oxygen consumption (BVO_2) was determined by PVA and E_{es} with high precision as follows [4]

$$BVO_2 = \alpha \cdot PVA + \beta \cdot E_{es} + \gamma \quad (6)$$

where α (1.8×10^{-5} mL O_2·mmHg^{-1}·mL^{-1}), β (1.8×10^{-3} mL O_2·mmHg^{-1}·mL), and γ (1.0×10^{-2} mL O_2) are constants. PVA stands for LV pressure-volume area (an index of total mechanical energy of LV contraction). PVA is the sum of LV stroke work (SW) and potential energy (PE). SW and PE are approximated as

$$SW = (P_m - P_{LA}) \cdot CO / HR \quad (7)$$

$$PE = P_{LA}^{\ 2} / 2E_{es} \quad (8).$$

Minute LV oxygen consumption per minute (MVO_2) and LV mechanical efficiency (ME) and are expressed as follows

$$MVO_2 = BVO_2 \cdot HR \quad (9)$$

$$ME = SW / BVO_2 = SW \cdot HR / MVO_2 \quad (10).$$

D. Simulation Results

Shown in Fig. 1 are simulation results. As explained in *subsection B*, there is an inverse relationship between E_{es} and heart rate [HR]. The top panel shows that if the heart is made bradycardiac, LV contractility should be enhanced to maintain P_m, CO, and P_{LA}, or to meet the peripheral demands.

The middle and the bottom panel show that ME would increase and MVO_2 would decrease by making heart bradycardiac up to a certain HR. Below this HR, however, rather ME would decrease and MVO_2 would increase with further decrease in HR. The differences in constants α, β and γ would change the optimal HR but would not change the basic relations show in Fig. 1.

E. Interpretation of the Simulation Results

As predicted by Eqs. 6 and 9, MVO_2 would largely be affected by HR. As MVO_2 is obtained by multiplying BVO_2 by HR, and as BVO_2 does not decrease much with HR, MVO_2 increases with HR.

In extreme bradycardiac condition, however, increase in E_{es} is so rapid, and the effect of increase in E_{es} overwhelmed the effect of HR.

ME is shown to be proportional to the reciprocal of MVO_2. Using, Eq. 7, the numerator of the right-hand side of Eq. 10, SW·HR is equal to $(P_m - P_{LA}) \cdot CO$ and is constant.

III. Animal Experiment

We reproduced a similar condition as the previous simulation and examined if the same results would be obtained in an animal experiment [5].

A. Methods

We used 7 dogs for this animal experiment. These dogs were anesthetized and underwent coronary micro-embolization with glass beads. This procedure resulted in acute ischemic heart failure. We adjusted the size and the

dose of the emboli, so as to create heart failure severe enough that necessitated an intensive care. In these dogs, CO decreased by 39% (from 101±5 to 62±13 ml·min^{-1}·kg^{-1}), P_m decreased by 17 mmHg (from 114±4 to 97±14 mmHg), and P_{LA} increased by 8 mmHg (from 9 ± 1 to 17±2 mmHg).

To take the full control of HR in hand, a specific bradycardiac agent zatebradine (0.5 mg·kg^{-1}) was administered intravenously, and the intrinsic atrial beats were suppressed. Then, HR is fully controlled by atrial pacing. We first set HR at the rate before zatebradine infusion (146±8 bpm). In this condition (designated as *untreated*), we measured hemodynamics and cardiac energetics.

We then activated the autopilot system [1] we developed to maintain the desired P_m, CO, and P_{LA}. We customized in each animal the target values for P_m, CO, and P_{LA}. These ranged between 90 to 100 mmHg for P_m, 80 to 100 ml·min^{-1}·kg^{-1} for CO, and 10 to 12 mmHg for P_{LA}. The system restored P_m, CO and P_{LA} to their respective target values within 30 min. After confirming stable hemodynamics, (designated as *treated for hemodynamics*), we measured hemodynamics and cardiac energetics.

After the treatment of hemodynamics, we then reduced the atrial pacing rate in steps of 10 or 20 bpm. For each HR step, we waited until the hemodynamics stabilized. . We were able to reduce HR by 39±12 bpm. We measured hemodynamics and cardiac energetics at the lowest HR and stable hemodynamics (designated as *treated for hemodynamics and energetics*).

B. Results

We summarized the results of the animal experiment in Fig. 2. In each panel we plotted the pooled relationships between HR and various indexes of hemodynamics and cardiac energetics, in 7 dogs.

In *Untreated* condition (shown by open circles), CO was lower and P_{LA} was higher than normal. P_m was not so different from normal values. HR was quite high due to the activation of sympathetic nervous system.

By activating the autopilot system (*Treated for Hemodynamics* condition, shown by solid triangle), CO and P_{LA} were restored to the target normal values. P_m was slightly decreased. Because we are fully controlling HR, and we did not change the setting of HR, HR remained high also in this condition.

After decreasing HR to the lowest level (*Treated for Hemodynamics and Energetics* condition, shown by solid circle), all of CO, P_{LA}, and P_m remained the target normal values despite the large decrease in HR (CO: 89 ± 3 ml·min^{-1}·kg^{-1} to 88 ± 3 ml·min^{-1}·kg^{-1}, P_{LA}: 10.5 ± 0.4 mmHg to 10.9 ± 0.4 mmHg, P_m: 94 ± 3 mmHg to 93 ± 2 mmHg, all NS).

As shown in the right upper panel, the treatment for hemodynamics required the enhancement of contractility (E_{es}, $p<0.05$ vs. *Treated for Hemodynamics*); this is accomplished by the automatic infusion of a positive inotropic agent (dobutamine, increased from 1.4 ± 0.3 to 2.7 ± 0.5 μg·min^{-1}·kg^{-1}, $p<0.01$). With a decrease in heart rate, it is shown that a further increase in contractility was necessary to maintain CO, P_{LA}, and P_m. Doses for other drugs were also changed to maintain hemodynamics.

Although ME increased with the treatment for hemodynamics, this was at the expense of increasing MVO_2. With the treatment of hemodynamics and energetics, however, we were able to maintain hemodynamics, further improving ME ($p<0.01$ vs. *Treated for Hemodynamics*), and at the same time decreasing MVO_2 almost at the untreated level or rather to a lower level ($p<0.01$ vs. *Treated for Hemodynamics*). Even though we were unable to study extreme bradycardiac condition, a similar relationships were obtained as the theoretical analysis up to the heart rate studied (i.e., minimal heart rate was not below the optimal heart rate for minimizing myocardial oxygen consumption).

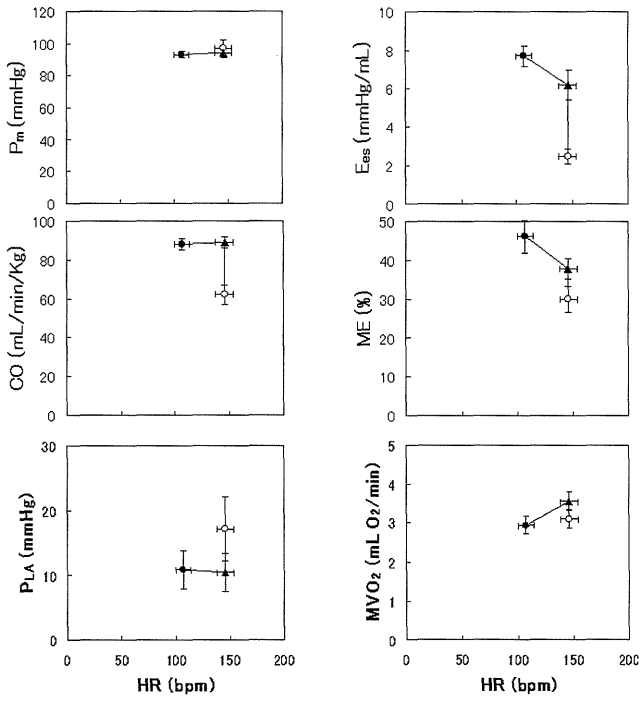

Fig. 2. Pooled relations between heart rate (HR) and mean blood pressure (P_m) (left top), cardiac output (CO) (left middle), left atrial pressure (P_{LA}) (left bottom), end-systolic elastance (E_{es}) (right top), left ventricular mechanical efficiency (ME) (right middle), and minute left ventricular oxygen consumption (MVO_2) (right bottom) in 7 dogs

IV. Conclusion

By taking full control of heart rate, and by adjusting treatment for hemodynamics at the same time, it was possible to maintain hemodynamics without sacrificing LV oxygen consumption.

REFERENCES

[1] K. Uemura, A. Kamiya, I. Hidaka, T. Kawada, S. Shimizu, *et al.*, "Automated drug delivery system to control systemic arterial pressure, cardiac output, and left heart filling pressure in acute decompensated heart failure," *J. Appl. Physiol.* vol. 100, no 4, 1278-1286, Apr. 2006.

[2] M. Sugimachi, K. Todaka, K. Sunagawa, M. Nakamura, "Optimal afterload for the heart vs. optimal heart for the afterload," *Front. Med. Biol. Eng.* vol. 2, no. 3, 217-221, 1990.

[3] K. Sunagawa, K. Sagawa, W. L. Maughan, "Ventricular interaction with the loading system," *Ann. Biomed. Eng.* vol. 12, no. 2, 163-189, 1984.

[4] H. Suga, "Ventricular energetics," *Physiol. Rev.* vol. 70, no. 2, 247-277, Apr. 1990.

[5] K. Uemura, K. Sunagawa, M. Sugimachi, "Computationally managed bradycardia improved cardiac energetics while restoring normal hemodynamics in heart failure," *Ann. Biomed. Eng.* vol. 37, no. 1, 82-93, Jan. 2009.

33rd Annual International Conference of the IEEE EMBS
Boston, Massachusetts USA, August 30 - September 3, 2011

Impact of baroreflex on venous return surface

Takafumi Sakamoto, Yoshinori Murayama, Atsushi Tanaka, Kazuo Sakamoto, Tomoyuki Tobushi, Keita Saku, Kazuya Hosokawa, Ken Onitsuka, Takeo Fujino and Kenji Sunagawa, Senior *Member, IEEE*

Abstract— **Background: Although Guyton's concept of venous return (VR) revolutionized circulatory physiology, the pulmonary circulation is invisible in its original framework. Since the pulmonary circulation is critical in left heart failure, we characterized the VR as a surface described by right (P_{RA}) and left atrial (P_{LA}) pressures and demonstrated that the VR surface was capable of representing mechanics of pulmonary as well as systemic circulation. However how baroreflex impacts the VR surface remains unknown. Methods/Results: In 8 dogs, we isolated the carotid sinuses and replaced both ventricles with pumps. We varied cardiac output, shifted blood distribution between the systemic and pulmonary circulation at carotid sinus pressures (CSP) of 100 or 140 mmHg. The coefficient of determination of the VR surface ranged 0.96-0.99 indicating how flat the surface is. Increasing CSP decreased maximum VR (233±27 vs. 216±33 ml/kg/min, $p<0.05$), whereas did not change the slopes of VR along P_{RA} or P_{LA} axes. Conclusions: Baroreflex parallel shifts the VR surface, thereby stressed volume, without changing its slopes.**

I. Introduction

Guyton's classic concept of circulatory equilibrium [1] revolutionized circulatory physiology. Guyton's classic concept, however, was not intended to represent the circulatory equilibrium of left ventricular failure because neither left ventricular mechanics nor pulmonary circulation is explicitly incorporated. To overcome such a limitation of Guyton's classic concept, we previously developed a framework of circulatory equilibrium [2, 3] where, as shown in Fig. 1, we defined the cardiac output curve and venous return curve as functions of both right atrial pressure (P_{RA}) and left atrial pressure (P_{LA}). We denoted the venous return curve as the venous return surface. A theoretical analysis using a distributed vascular model indicated that venous return (VR) of the total circulatory system can be described as

$$VR=VR_{max}-(G_P P_{LA}+G_S P_{RA}) \qquad (1)$$

where VR_{max} is maximum venous return and is a function of stressed blood volume [2, 3, 4], G_P and G_S, conductance of pulmonary and systemic venous return, respectively. We demonstrated that the venous return surface was remarkably flat and the slopes toward the P_{LA} and P_{RA} axes did not differ among animal preparations [2, 3].

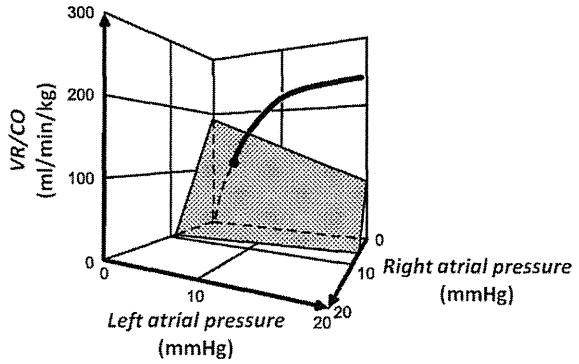

Figure 1 Proposed framework of circulatory equilibrium consists of integrated cardiac output curve and venous return surface.

Since baroreflex is a powerful physiological modulator of mechanical properties of cardiovascular system and thereby capable of changing circulatory equilibrium, we investigated how baroreflex impacts on characteristics of venous return surface.

II. Methods

A. Animal preparation

Eight mongrel dogs were anesthetized with pentobarbital sodium and ventilated artificially. We isolated the bilateral carotid sinuses from the systemic circulation and connected them to a servo-controlled piston pump to control intra-carotid sinus pressure (CSP). We cut the bilateral vagosympathetic trunks to eliminate other reflexes. After median sternotomy, the heart was suspended in a pericardial cradle. Fluid-filled catheters were placed in the right and left atrium to measure pressures.

To examine the venous return surface, we performed total heart bypass. Two roller pumps were used to control systemic and pulmonary flows. A systemic perfusion cannula was placed in the right common carotid artery. A draining cannula for the systemic circulation was inserted into the right ventricle through its free wall. A pulmonary perfusion cannula was placed in the pulmonary artery. A draining cannula for pulmonary circulation was inserted into the left ventricle via the apex. The flow rate (i.e., cardiac output) was measured by an in-line ultrasonic flow probe. After starting two roller pumps at a matched rate, we tied an umbilical tape around pulmonary artery, clamped the ascending aorta and thus established the total heart bypass.

B. Protocol

For a given CSP, we waited for several minutes until the

Manuscript received September 15, 2011. This work was supported in part by Health and Labour Sciences Research Grant for Research on Medical Devices for Improving Impaired QOL from the Ministry of Health Labour and Welfare of Japan, Health and Labour Sciences Research Grant for Clinical Research from the Ministry of Health Labour and Welfare of Japan, and Grant-in-Aid for Scientific Research(S) (18100006) from the Japan Society for the Promotion of Science

All authors are with Kyushu University, Fukuoka 8128582 Japan. (corresponding author Takafumi Sakamoto to provide phone: +81-92-642-5360; fax: +81-92-642-5357; e-mail: tsaka@cardiol.med.kyushu-u.ac.jp).

hemodynamic conditions reached a steady state. We then simultaneously changed the flow rate of both pumps stepwise between 40 and 100 ml/min/kg in an increment of 20ml /min/kg. In each step, we varied the blood volume distribution between the pulmonary and the systemic circulations by transiently unbalancing the flow rates of the two pumps. We conducted the protocol at CSP of 100 and 140 mmHg.

III. Results

We applied multivariate regression analysis and determined VR_{max}, G_P and G_S. Shown in the left panel of Fig. 2 is a representative venous return surface. All data points appear to be distributed on a flat surface. The fact that all points are distributed around a single line if they are viewed from a direction parallel to the surface indicated how flat the surface is (not shown). Baroreflex did not affect the flatness of the venous return surface. The multiple correlation coefficient was close to unity (r2=0.96-0.99) suggesting that the venous return surface is reasonably flat in every animal.

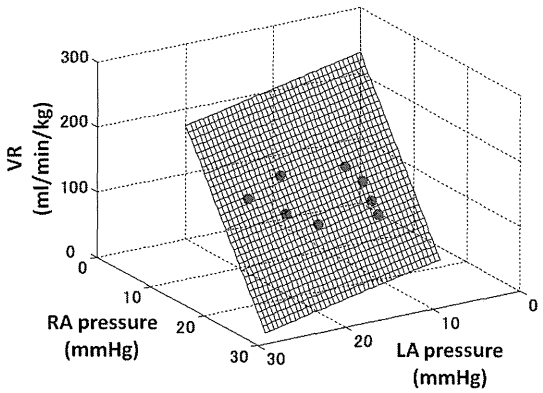

Figure 2 Representative venous return surface at CSP 140mmHg

Illustrated in Fig. 3 are the impact of baroreflex on VR_{max}, G_S and G_P. Increasing CSP significantly decreased VR_{max}, (233±27 vs. 216±33 ml/kg/min, data were means ± SD, $p<0.05$, paired t-test) whereas it did not change G_P or G_S. This is to say that baroreflex shifted the VR surface along the vertical axis without changing the slopes. Since the VR_{max} reflects stressed blood volume [2, 3], baroreflex in turn changed stressed blood volume.

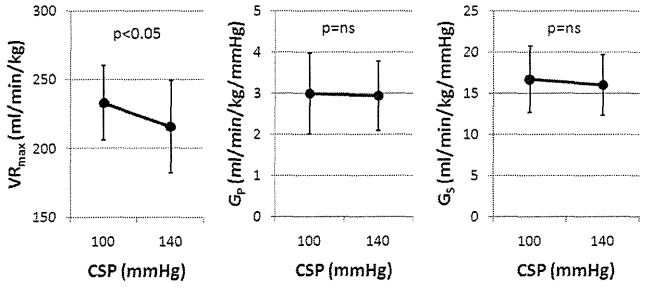

Figure 3 VR_{max}, G_P, and G_S obtained at CSP 100 and 140 mmHg

IV. Discussion

Uemura et al [2, 3] have demonstrated that VR surface was remarkably flat and the slopes toward P_{LA} and P_{RA} axes did not differ among animal preparations. But the impact of baroreflex on VR surface remained unknown. We reconfirmed that the venous return surface is reasonably flat over a wide range of cardiac output and venous pressures. Baroreflex did not affect the flatness of the venous return surface. Baroreflex markedly changes the maximum venous return, thereby stressed volume, but did not change the slopes of the venous return surface.

V. Conclusion

We conclude that baroreflex modulates the circulatory equilibrium by changing the stressed blood volume without affecting the slopes of venous return.

Acknowledgment

This study was supported in part by Health and Labour Sciences Research Grant for Research on Medical Devices for Improving Impaired QOL from the Ministry of Health Labour and Welfare of Japan, Health and Labour Sciences Research Grant for Clinical Research from the Ministry of Health Labour and Welfare of Japan, Grant-in-Aid for Scientific Research(S) (18100006, 23220013) from the Japan Society for the Promotion of Science.

References

[1] A.C. Guyton, "Textbook of Medical Physiology", *1956.*

[2] K. Uemura, M. Sugimachi, T. Kawada, A. Kamiya, Y. Jin, K. Kashihara, and K. Sunagawa, "A novel framework of circulatory equilibrium," *Am J Physiol Heart Circ Physiol 286: H2376-H2385, 2004.*

[3] K. Uemura, T. Kawada, A. Kamiya, T. Aiba, I. Hidaka, K. Sunagawa, and M. Sugimachi, "Prediction of circulatory equilibrium in response to changes in stressed blood volume," *Am J Physiol Heart Circ Physiol 289: H301-H307, 2005.*

[4] K. Sagawa, L. Maughan, H. Suga, K. Sunagawa, "Cardiac Contraction and Pressure-Volume Relationship," *Oxford Univ. Press, p. 232-298, 1988.*

33rd Annual International Conference of the IEEE EMBS
Boston, Massachusetts USA, August 30 - September 3, 2011

Experimental 'Jet Lag' Causes Sympathoexcitation via Oxidative Stress through AT_1 Receptor in the Brainstem

T. Kishi, K. Sunagawa

***Abstract*- Circadian disruptions through frequent transmeridian travel, rotating shift work, and poor sleep hygiene are associated with an array of physical and mental health maladies, including the abnormal autonomic nervous system. We have demonstrated that the oxidative stress through AT_1 receptor in the brain activates sympathetic nervous system. The aim of the present study was to determine whether experimental 'jet lag' causes sympathoexcitation via oxidative stress through AT_1 receptor in the cardiovascular center of the brainstem (rostral ventrolateral medulla; RVLM) or not. Experimental 'jet lag' was made to normotensive (Wister-Kyoto rat; WKY rat) and hypertensive rats (stroke-prone spontaneously hypertensive rats; SHRSP) by the exposure to a 12 hour phase advance for 5 days. In WKY, 'jet lag' increases blood pressure and the activity of sympathetic nervous system via oxidative stress through angiotensin II type 1 receptor in the RVLM for 2 days only, and the changes are improved at 3 day after the initiation of 'jet lag'. In SHRSP, 'jet lag' also increases blood pressure and the activity of sympathetic nervous system via oxidative stress through angiotensin II type 1 receptor in the RVLM, and the changes are greater compared to those in WKY, and are maintained for the period of 'jet lag'. These results suggest that experimental 'jet lag' causes sympathoexcitation via oxidative stress through AT_1 receptor in the brain, especially in hypertension.**

INTRODUCTION

Frequent transmeridian travel is known to cause an disturbance in circadian timing system [1, 2]. This disturbance is associated with a number of clinical pathologies, including a higher incidence of hypertension and cardiovascular disease [3, 4]. In mammals, the master circadian pacemaker is located in the suprachiasmatic nucleus (SCN) in the anterior hypothalamus, and the SCN generates endogenous oscillations with a period of approximately 24 hours [5]. At the cellular level, circadian rhythms are generated by 24-hour autoregulatory transcriptional feedback loops consisting of 'clock' genes and their protein products [6]. A recent study suggests that the circadian disruption lead to marked suppression of hippocampal cell proliferation and neurogenesis, associated with notable deficits in learning and memory [7].These results indicate that 'jet lag' causes the changes in neural structures and functions in the brain. In terms of the regulation of blood pressure and heart rate via sympathetic nervous system, central nervous system involved in baroreflex circuit is important [8]. However, it has not been determined whether the abnormalities in blood pressure and heart rate in 'jet lag' are due to the changes in central nervous system or not.

We have demonstrated that nitric oxide and oxidative stress in the brainstem regulates the activity of the sympathetic nervous system [9, 10]. Especially, in the brainstem, oxidative stress through the angiotensin II type 1 receptor in the rostral ventrolateral medulla (RVLM) causes the sympatho-excitation [11]-[13]. Taken together, we hypothesize that 'jet lag' might cause hypertension through the sympathoexcitation due to the oxidative stress in the RVLM. However, the mechanisms in which 'jet lag' causes hypertension or sympathoexcitation have not been fully determined.
The aims of the present study was to determine whether the experimental 'jet lag' causes sympathoexcitation or not, and if so, whether the experimental 'jet lag'-induced sympathoexcitation is due to the oxidative stress through AT_1 receptor in the RVLM or not. To do these aims, we made the experimental 'jet lag' model rats by the exposure to a 12 hour phase advance for 5 days.

PROCEDURES

Ethics statement

This study was reviewed and approved by the committee on ethics of Animal Experiments, Kyushu University Graduate School of Medical Sciences, and conducted according to the Guidelines for Animal Experiments of Kyushu University.

Animals

Adult male stroke-prone spontaneously hypertensive rats (SHRSP) and Wister-kyoto (WKY) rats maintained on a 14:10 light:dark (LD) cycle (Lights on at 0700 h) prior to the onset of the experiments, with a light

Manuscript submitted April 15, 2011, revised manuscript submitted June 20, 2011.

T. Kishi is with the Department of Advanced Therapeutics for Cardiovascular Diseases, Kyushu University Graduate School of Medical Sciences, Fukuoka, 812-8582 Japan (phone: +81-92-642-5360; fax: +81-92-642-5374; e-mail: tkishi@cardiol.med.kyushu-u.ac.jp).

intensity ranging from 100-300 lux at the level of each cage. All animals were maintained in a colony room and provided with ad libitum access to water and food.

Experimental 'Jet Lag'

WKY and SHRSP were divided into two groups, 'jet lag'-WKY, control-WKY, 'jet lag'-SHRSP, and control-SHRSP. 'Jet lag'-WKY and –SHRSP groups were exposed to a 12 hour phase advance for 5 days, while control-WKY and –SHRSP groups were remained in a 14:10 LD (lights on at 0700 hr) cycle for the same duration.

Measurement of Blood Pressure and Heart rate

The UA-10 telemetry system (Data Sciences International) was used to measure mean arterial pressure and heart rate. The surgical procedure has been described previously [9, 11]. Mean arterial pressure and heart rate were recorded continuously for 10 minutes every day in light and dark phase by a multichannel amplifier and signal converter.

Urinary Norepinephrine Excretion As an Parameter of the Activity of Sympathetic Nervous System

As the parameter of the activity of the sympathetic nervous, we measured the urinary norepinephrine concentration by high-performance liquid chromatography (HPLC), and calculated the urinary norepinephrine excretion for 24 hours [9]-[13].

Oxidative Stress in the RVLM

As an indicator of the oxidative stress in the RVLM, we measured thiobarbituric acid-reactive substances (TBARS) levels in the tissues obtained from the RVLM of each group at the end of the study as described in previous studies [11]-[13]. Moreover, to determine the TBARS levels in the RVLM at 2 day after the initiation of 'jet lag', we made the other 4 groups, 'jet lag' for 2 days-WKY, control-WKY, 'jet lag' for 2 days-SHRSP, and control-SHRSP.

Microinjection of Angiotensin II Type 1 Receptor Blocker into the RVLM

To inhibit the angiotensin II type 1 receptor in the RVLM locally, we microinjected losartan (1nmol), angiotensin II type 1 receptor blocker, into the bilateral RVLM of each group at the end of the study. Moreover, to determine the activity of the angiotensin II type 1 receptor in the RVLM at 2 day after the initiation of 'jet lag', we made the other 4 groups, 'jet lag' for 2 days-WKY, control-WKY, 'jet lag' for 2 days-SHRSP, and control-SHRSP. Each rat was anesthetized with sodium pentobarbital. A catheter was inserted into the femoral artery to record arterial blood pressure. A tracheal cannula was connected to a ventilator, and the rats were artificially ventilated. The rats were placed in a stereotaxic frame. The identification of the RVLM and the procedures of the microinjection were confirmed as described previously [11]-[13].

RESULTS

Blood Pressure and Heart rate

Fig.1 shows the results of mean arterial pressure. Prior to the experiments, mean arterial pressure and heart rate were significantly higher in SHRSP than in WKY both at light and dark phase (Fig. 1 and 2). For the rats, light phase is a rest phase, and dark phase is an active phase. In dark and light phase, mean arterial pressure and heart rate were significantly higher in 'jet lag'-WKY than in control-WKY at 1-2 day after the initiation of 'jet lag', and was similar in 'jet lag'-WKY and control-WKY at 3-5 day after the initiation of 'jet lag' (Fig. 1 and 2). In dark phase, mean arterial pressure and heart rate were similar in 'jet lag'-SHRSP and control-SHRSP (Fig. 1 and 2). However, in light phase, mean arterial pressure and heart rate were significantly higher in 'jet-lag'-SHRSP than in control-SHRSP for the 'jet lag' period (Fig. 1 and 2).

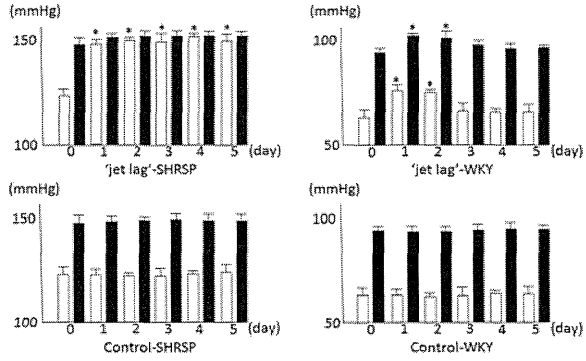

Fig 1. The results of mean arterial pressure in each group. White column indicates light phase, and black column indicates dark phase. N=5 for each. *P<0.05 vs control.

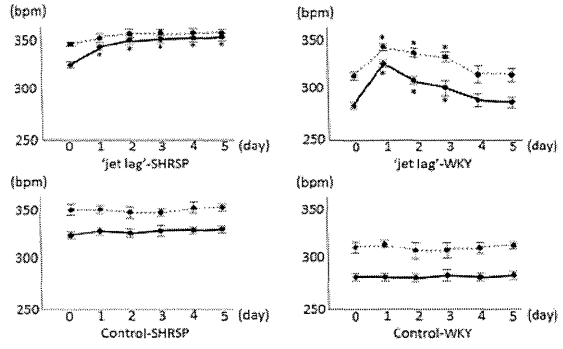

Fig 2. The results of the averages of heart rate in each group. Solid line indicates light phase, and dot line indicates dark phase. N=5 for each. *P<0.05 vs control.